

# Spectroelectrochemical Analysis of the Electrochromism of Antimony-Doped Nanoparticulate Tin–Dioxide Electrodes

Malte Pflughoeft<sup>†</sup> and Horst Weller\*

Contribution from the Institute of Physical Chemistry, University of Hamburg, Bundesstrasse 45, D-20146 Hamburg, Germany

Received: February 22, 2002; In Final Form: June 28, 2002

A new synthesis of alcohol-soluble antimony-doped tin dioxide nanoparticles is described. The spectroelectrochemical behavior of nanocrystalline thin film electrodes prepared by dip coating from the colloidal solutions is investigated, and the applicability as an electrochromic device is demonstrated. Coloration results from light absorption by free electrons and Sb(III)–Sb(V) charge-transfer transitions. The ratio of free electron and charge-transfer absorption is determined by the distribution of antimony dopant atoms within the SnO<sub>2</sub> host lattice. The latter can be controlled applying different precursors and reaction conditions during the synthesis of the nanoparticles.

## Introduction

Electrochromic devices undergo a color change by electrochemically induced redox processes of the electrode material. In conventional electrochromic layers, charge injection is compensated by ion insertion into the electrode. This process is one of the rate-determining steps, because a diffusion of ions in solids is a slow process. Moreover, multiple insertion cycles are accompanied by substantial lattice stress, which leads to mechanical decomposition of the electrodes. Nanoparticulate thin film electrodes can overcome these problems because the charge compensation can be fully achieved by charging and discharging the electrical double-layer of the inner surface of these spongelike structures. Recently, the electrochromic behavior of antimony-doped nanoparticulate SnO<sub>2</sub> films was discovered.<sup>1,2</sup> Coloration of antimony-doped SnO<sub>2</sub> electrodes is mainly due to free electron absorption, tunable by the dopant concentration and, thus, the number density of free electrons. This is in accord to Drude–Mie theory. The optical properties of the antimony-doped SnO<sub>2</sub> films were described after modeling the charging of the space charge layer using a Mott–Schottky-like treatment. Zum Felde et al. also showed the existence of an additional absorption process explained in terms of Sb(III)–Sb(V) charge-transfer processes that lead to enhanced coloration in the visible range.

Energy-dependent synchrotron XPS analysis on Sb-doped SnO<sub>2</sub> particles were also reported,<sup>3,4</sup> it was shown that depending on preparation conditions, antimony-doped SnO<sub>2</sub> particles show different dopant profiles of Sb(III) and Sb(V).

Here we report on in situ spectroelectrochemical properties of electrodes made from antimony-doped SnO<sub>2</sub> particles and correlate their spectroelectrochemical response with their dopant profiles. Moreover, we also describe improvements on the former synthetic procedures for nanoparticulate films that allow use of dip coating (a technique allowing homogeneous coating of curved surfaces).

## Experimental Section

**Preparation of Colloidal Solution.** A 30.6 g (87.3 mmol) sample of SnCl<sub>4</sub>·5H<sub>2</sub>O (Riedel-de Haën) was dissolved in 500 mL of H<sub>2</sub>O (Millipore, 18.2 MΩ/cm). SbCl<sub>3</sub> or SbCl<sub>5</sub> (Merck, p.A.) was dissolved in 10 mL of 37% HCl (Merck, p.A.), and the resulting solution was added to the tin chloride solution. After stirring for 1 h, the solution was neutralized by addition of 25% ammonia (Merck, p.A.). The resulting precipitate was centrifuged at 3100g, washed six times with water, washed two times with 2-propanol (Merck, p.A.), and dissolved in 20 g of a 25 wt % solution of (C<sub>4</sub>H<sub>9</sub>)<sub>4</sub>NOH (20 mmol) in methanol (Fluka, pract.), and the resulting solution was filled to 100 mL with 2-propanol and stirred overnight.

For chlorine free samples 8.223 g (20 mmol) of Sn(O-*t*-Bu)<sub>4</sub> (Gelest) and 1.364 g (4 mmol) of Sb(O-*n*-Bu)<sub>3</sub> (Gelest) were dissolved in 100 mL of H<sub>2</sub>O (Millipore, 18.2 MΩ/cm) under addition of HClO<sub>4</sub> (70 wt %, Merck, p.A.). The rest of the synthesis is analogous to the synthesis described above. The precipitate was dissolved in 6.3 g (25 wt %) of a solution of (C<sub>4</sub>H<sub>9</sub>)<sub>4</sub>NOH (20 mmol) in methanol (Fluka, pract.), and the resulting solution was filled to 20 mL with 2-propanol and stirred overnight. Chlorine could not be found in the sample by X-ray fluorescence analysis.

**Analytical Methods.** Quantitative analysis of antimony and tin was performed using atomic absorption spectroscopy (AAS) and atomic emission spectroscopy (AES); quantitative analysis of chloride was performed using by X-ray fluorescence analysis.

For thermogravimetric analysis (TG) the sample was heated in air at a rate of 3 °C/min. The resulting gaseous products were analyzed by mass spectroscopy.

**Preparation of Electrodes.** The electrodes were prepared by dip coating of glass slides (TEC 15, LOF Libbey-Owens-Ford). The films were dried for several minutes at room temperature (RT), 60 °C, 150 °C, and finally 500 °C. After the films were cooled to room temperature, the coating procedure was repeated three times. Cu wires were affixed to the conducting surface of the glasses using silver epoxy resin (Epoxy Produkte). The exposed Ag and the Cu wires were insulated with two-component epoxy glue (Pattex).

\* Corresponding author. E-mail: weller@chemie.uni-hamburg.de.

<sup>†</sup> Present address: Department of Chemistry and Biochemistry, 607 Charles E. Young Dr. East, University of California at Los Angeles (UCLA), Los Angeles, CA 90095. E-mail: pflughoe@chem.ucla.edu.

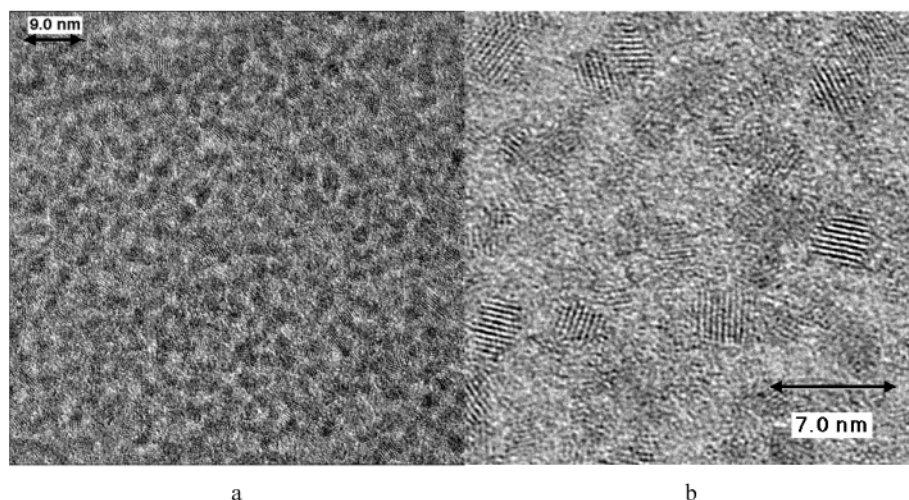


**Figure 1.** HRTEM images of 20%  $\text{SnO}_2\text{:Sb}$ : (a) nanoparticles deposited from colloidal solution; (b) nanoparticulate film heated to 500 °C.

**Apparatus.** Transmission electron microscopy (TEM) images were collected using a Philips CM300UT microscope operating at 300 kV. The microscope was equipped with a  $\text{LaB}_6$  cathode, EDX detector (EDAX), and a CCD camera (Gatan 694). Optical spectra were recorded using a Cary 500 (Varian) UV/vis/NIR spectrophotometer. Spectroelectrochemical measurements were performed in a custom quartz cell with 50  $\mu\text{m}$  electrolyte optical path length. Spectra were measured against air. A silver/silver chloride ( $\text{Ag/AgCl/KCl}$  3 (mol/L)) reference electrode (RE) and a platinum counter electrode (CE) were mounted close to the working electrode, all potentials quoted relate to RE. The electrical potential was generated by a potentio-galvano-scan generator Wenking PGS81R and observed with an HP34401A multimeter. The current was detected by an oscilloscope Voltcraft PCS32i. Powder X-ray patterns were measured with a Philips Xpert or a Bruker AXS D8 Advance diffractometer. Simultaneous thermogravimetry (TG), differential thermal analysis (DTA), and mass spectroscopy (MS) of evolved gases were carried out with a Netzsch STA 409/Balzers QMS 421 system in dynamic air atmosphere. Samples were placed in open aluminum crucibles. X-ray fluorescence analysis was performed using a Philips PW 1220. IR spectra were recorded on a Bruker Equinox 55.

Photoemission experiments were performed at the Undulator beamline BW3 at HASYLAB/DESY, equipped with a SX700 monochromator, which generates photons in the 100–1200 eV range. Measurements were made using an Omicron EA125 hemispherical energy analyzer (HEA) for acquiring the photoemission spectra. By varying the photon energy, one can vary the sampling depth.

## Results

Figure 1 shows TEM images of 20% antimony-doped  $\text{SnO}_2$  particles before and after heating for 1 h at 500 °C. During this process, the particles grow from approximately 2.5 nm (Figure 1a) to 5–6 nm (Figure 1b); see also XRD pattern in Figure 2. Debye–Scherrer analysis reveals an average particle size of 2.1 nm before heating and 4.0 nm after heating, consistent with the TEM data. The particles crystallize in the thermodynamically stable, bulk-phase cassiterite (Figure 2). For lower dopant concentration, the particles grow slightly larger; for example, 2%  $\text{Sb}^{3+}$ -doped nanoclusters grow up to 6–7 nm.

To elucidate the processes during heating of the films, we have examined mass spectrometry-coupled thermal analysis of 20%  $\text{Sb}^{3+}$ -doped  $\text{SnO}_2$  particles. The DTA signal during heating

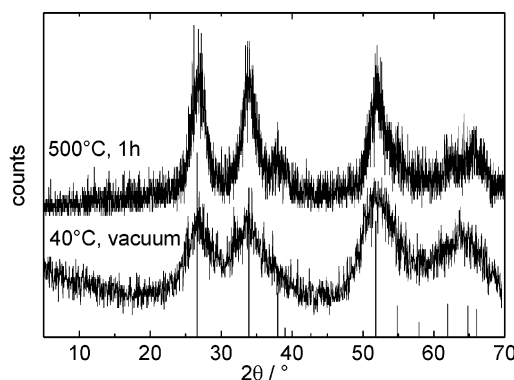


**Figure 2.** X-ray diffraction pattern of 20%  $\text{SnO}_2\text{:Sb}$ , dried in a vacuum and heated to 500 °C. Solid lines indicate the reflexes of bulk phase cassiterite.

(solid line in the upper panel of Figure 3), six main processes, indicated 1–6, can be observed: processes 1 and 2 are seen to be endothermic, and 3–6 are exothermic. The differential mass loss curve (broken line in the upper panel of Figure 3) is also shown and also six main processes are observable at the same positions in temperature. For more detailed information about the thermally induced processes, we have plotted the corresponding mass spectrometric data at selected  $m/e$  values in the lower part of Figure 3. A detailed discussion of the six processes will be given below.

Absorption spectra were measured at various electrode potentials for 20%-doped  $\text{SnO}_2$  (Figure 4, panel a) and 2%-doped  $\text{Sb}^{3+}$  (Figure 4, panel b) electrodes. We have plotted these spectra as differences to the absorption spectra recorded at +1.2 V electrode potential, which are almost identical with the blank spectra of the uncoated TEC glass except for interference patterns caused by the film thickness and a very small residual NIR absorbance in the case of the 20%-doped films.

In Figure 5 these spectra are depicted normalized at their corresponding maxima.

The general trend in all these spectra is the appearance of an absorption band in the NIR, which increases with negative potential. For 20%  $\text{Sb}^{3+}$ -doped electrodes (Figures 4a and 5a), the NIR band increases up to −0.2 V and decreases at more negative potentials. Concomitantly, a new absorption band arises in the visible. The absorption tail toward the IR region flattens with increasing negative potential, whereby the absorption maximum remains constant in the entire potential range. The 2%  $\text{Sb}^{3+}$ -doped sample shows a different behavior (Figures 4b

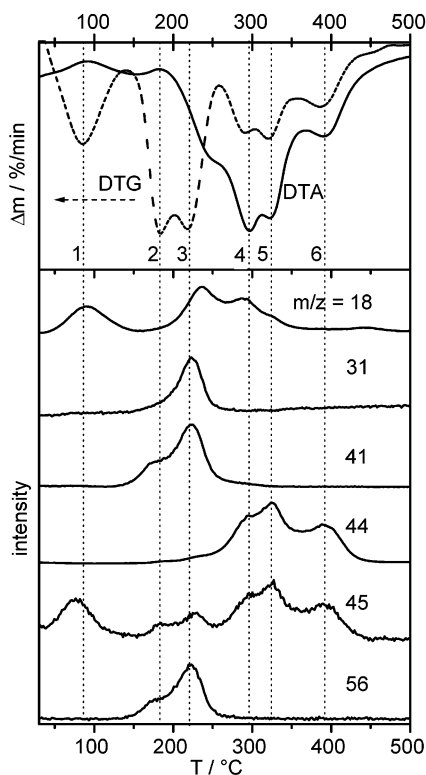


**Figure 3.** Results from thermal analysis: DTA, DTG, and MS signals.

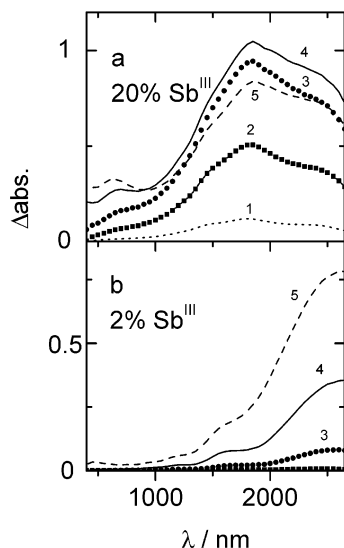


**Figure 4.** Potential-dependent absorption spectra of  $\text{SnO}_2\text{:Sb}$  electrodes (1 = +1 V, 2 = +0.6 V, 3 = +0.2 V, 4 = -0.2 V, 5 = -0.6 V): (a)  $\text{SnO}_2\text{:Sb}$  20%; (b)  $\text{SnO}_2\text{:Sb}$  2%.

and 5b), with its absorption maximum shifting to longer wavelengths, its shape of the spectra remaining constant in the entire potential range, and its spectral changes starting at 0.4 V instead of 1 V for the 20%  $\text{Sb}^{3+}$ -doped sample. Because the absorption maximum occurs at the very end of the spectral window of our UV/vis/NIR spectrometer, we repeated this measurement on an FTIR spectrometer with an identical dry electrode prepared on a sapphire window. The exact position of the maximum was 3300 nm.

We attribute the broad NIR band to free-charge-carrier absorption within the conduction band of the nanoparticles and the additional absorption band in the vis to the absorption of a charge-transfer band of an  $\text{Sb}^{3+}\text{--Cl}^-\text{--Sb}^{5+}$  complex.

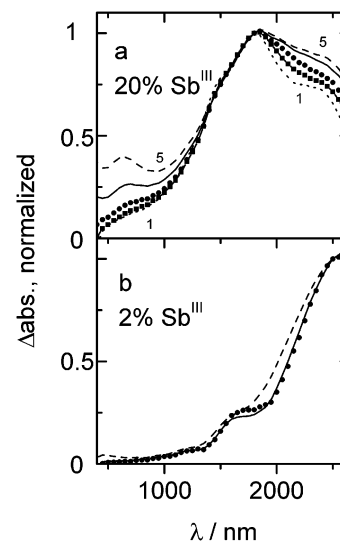


**Figure 5.** Potential-dependent absorption spectra of  $\text{SnO}_2\text{:Sb}$  electrodes between +1 and -0.6 V, normalized at the absorption maxima in the NIR region: (a)  $\text{SnO}_2\text{:Sb}$  20%, normalized at 1850 nm; (b)  $\text{SnO}_2\text{:Sb}$  2%, normalized at 2500 nm.

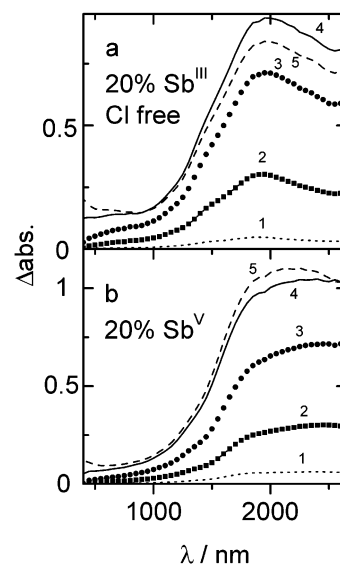


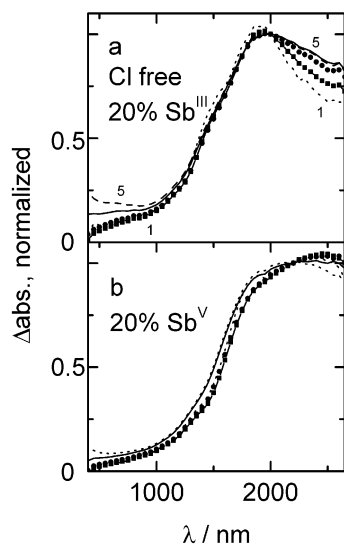
**Figure 6.** Potential-dependent absorption spectra of  $\text{SnO}_2\text{:Sb}$  electrodes (1 = +1 V, 2 = +0.6 V, 3 = +0.2 V, 4 = -0.2 V, 5 = -0.6 V): (a)  $\text{SnO}_2\text{:Sb}$  20%, chlorine free; (b)  $\text{SnO}_2\text{:Sb}$  20%,  $\text{Sb}^{5+}$  as precursor.

In Figures 6 and 7 we present the spectroelectrochemical results from samples prepared in the absence of  $\text{Cl}^-$  (panel a) from samples obtained by doping with  $\text{Sb}^{5+}$  (panel b).

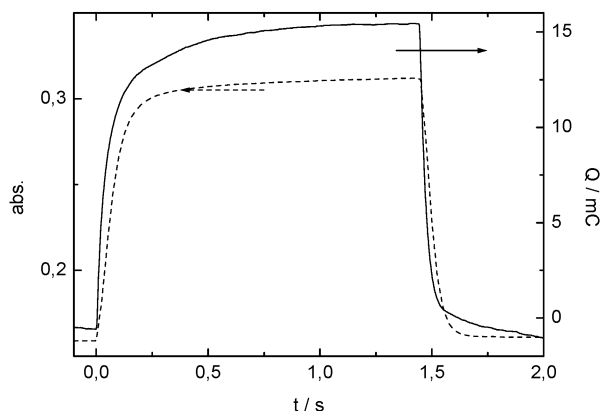
In the  $\text{Cl}^-$ -free 20%  $\text{Sb}^{3+}$  sample the decrease of the NIR band and the appearance of the VIS band at most negative potentials is less pronounced than in the case of the  $\text{Cl}^-$ -containing 20%  $\text{Sb}^{3+}$  sample. This spectral feature is even absent in the 20%  $\text{Sb}^{5+}$  sample. In this sense, the 20%  $\text{Sb}^{5+}$  sample is more similar to the 2%  $\text{Sb}^{3+}$  sample, whereas the NIR absorption maximum is the same as that of the other 20%  $\text{Sb}$ .

Figure 8 shows the time dependence of the absorption signal at 650 nm and the charges obtained by integration of the current. At  $t = 0$ , the potential was abruptly changed from +1.2 V to -0.6 V, and after about 1.5 s, the potential was switched back. In Figure 8, an asymmetric form of the response can be seen. The decoloration is a much faster process than the coloring.





**Figure 7.** Potential-dependent absorption spectra of  $\text{SnO}_2\text{:Sb}$  electrodes between +1 and −0.6 V, normalized at the absorption maxima in the NIR region: (a) normalized at 2000 nm; (b) normalized at 2200 nm.

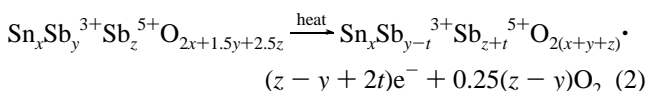
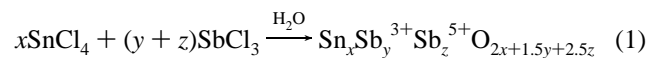


**Figure 8.** Time response of a nanoparticulate electrode after applying rectangular potential pulse (from +1.2 and −0.6 V at  $t = 0$  s and reverse to +1.2 V at  $t = 1.5$  s): (full line) deposited charge; (dotted line) absorbance change at  $\lambda = 650$  nm.

## Discussion

The preparation of nanostructured antimony-doped  $\text{SnO}_2$  films has already been described.<sup>5–7</sup> Film formation using aqueous colloidal solutions were used for screen printing,<sup>8</sup> and spin coating<sup>1,9,10</sup> was also described. We have developed a synthesis of alcoholic colloidal solution of antimony-doped tin dioxide with various antimony contents. The advantage of using alcoholic solutions is the ability to use dip coating processes for film formation. This technique allows the thin film formation even on curved substrates with high optical quality.

The observed growth upon heating to 500 °C and n-doping of the material is similar to that described by zum Felde.<sup>2</sup> Antimony incorporation and n-doping was described by the following reactions:



n-doping results from oxygen deficiencies electrostatically compensated by  $\text{Sb}^{5+}$  species on  $\text{Sn}^{4+}$  lattice sites. Each  $\text{Sb}^{3+}$

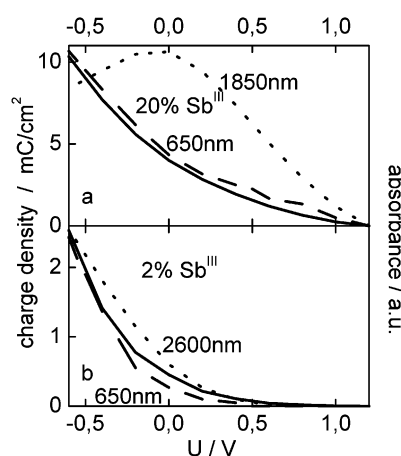


**Figure 9.** Comparison of charge density of the electrode (solid lines) with the absorption at 650 nm (dashed lines) and at the NIR maxima (dotted line).

neutralizes the effect of one  $\text{Sb}^{5+}$ . For dried colloids it was found that, after heating,  $\text{Sb}^{3+}$  and  $\text{Sb}^{5+}$  were present in a ratio of approximately 1:3 in the doping ranges 10 and 20% and independent of the oxidation state of the Sb precursor.<sup>11</sup>

Besides particle growth and doping, condensation of OH groups on the particle surfaces and oxidation of the organic compounds yielding  $\text{CO}_2$  occur under heating. The latter two processes can be detected by thermal analysis (Figure 3). The first endothermic process at ~90 °C represents the evaporation of 2-propanol and water (seen in the lower panel of the Figure 3,  $m/z$  18 (water) and 45 (1-hydroxyethyl, fragment of 2-propanol)). The second process at ~160 °C can be correlated to the elimination of butene from the tetrabutylammonium cation, which is an endothermic process as well ( $m/z$  41 (butene fragment) and 58 (butene)). This elimination reaction can also be correlated to the third process at ~220 °C, but here it is overlapped by the condensation of hydroxy and alkoxy groups, as can be seen by the loss of alcohols and water ( $m/z$  18, 31 (methanol) and 45(1-hydroxyethyl, fragment of 2-propanol)). This condensation process is exothermic. At ~300 °C the second condensation starts ( $m/z$  18 and 45). The final oxidation to carbon dioxide mainly takes place during processes 5 and 6 but starts already in process 4. The condensation at ~220 °C is attributed to the condensation of surface OH groups, whereas the second one at ~300 °C is assigned to interparticle condensation at the grain boundaries. This assignment is supported by the observation that films heated for longer times below 300 °C, before final firing at 500 °C, yielded samples with very poor optical and mechanical properties; i.e., the condensation at the particle surfaces was probably finished before the temperature was applied that was necessary to interconnect the particles to a stable network.

The in situ spectroelectrochemical measurements in the UV–vis and NIR range allow an insight into potential-dependent processes and the corresponding redox chemistry. In Figure 9 we have summarized characteristic spectral data and information on charge deposited at the respective potentials, as obtained from potential jump experiments. For the 20% antimony-doped  $\text{SnO}_2$  (Figure 9a) the optical absorption at 1850 nm follows the charge curve only up to 0 V. For negative potentials the NIR absorbance decreases again whereas the 650 nm absorbance further increases. We attribute the signal at 1850 nm to the plasmon absorption of free charge carriers.<sup>1,2</sup> The conduction band electrodes reduce some lattice species under negative polarization, which then absorb at 650 nm. The absorption coefficient

of this species approximates that of the free electrons at 650 nm, because the 650 nm absorbance curve directly follows the charge density curve over the entire potential range. As mentioned earlier, we attribute the 650 nm absorption to the existence of an  $\text{Sb}^{3+}\text{Cl}^{-}\text{Sb}^{5+}$  charge-transfer complex. Such complexes with similar absorption spectra were reported.<sup>12–14</sup> Formation of such a complex is not observed at low doping (2%  $\text{Sb}^{3+}$ , Figure 9b), possibly due to the low probability of finding two Sb directly interconnected by  $\text{Cl}^{-}$ . Recent energy dispersive XPS<sup>3,4</sup> has shown that the Sb distribution within the nanoparticles strongly depends on the doping concentration and the oxidation state of the Sb precursor. Up to 5% Sb ( $\text{Sb}^{3+}$  precursor) a homogeneous distribution of dopant atoms was found, which is consistent with the bulk solubility of Sb in  $\text{SnO}_2$ . For 20% Sb ( $\text{Sb}^{3+}$  precursor) doping, a strong enrichment of  $\text{Sb}^{3+}$  was observed in the outer shell of the nanoparticles, whereas in the core of the nanoparticle,  $\text{Sb}^{5+}$  with typical concentrations of 10% was detected. Thus, for high doping concentrations phase segregation leads to a gradient core–shell-like structure. This effect was not observed in the 20% Sb ( $\text{Sb}^{5+}$  precursor) sample, where a more homogeneous distribution was found, explained by the different ion radii, i.e., only  $\text{Sb}^{5+}$  can substitute a  $\text{Sn}^{4+}$  at a lattice site. In the latter case, the solubility of Sb within a  $\text{SnO}_2$  nanoparticle exceeds that of the bulk material. Therefore we believe that formation of the  $\text{Sb}^{3+}\text{Cl}^{-}\text{Sb}^{5+}$  charge-transfer complexes requires a core–shell-like phase segregation, plausible due to the higher probability of finding two Sb in the immediate vicinity.

For chloride-free samples, a somewhat weaker charge-transfer complex component was observed, explained by the formation of similar  $\text{Sb}^{3+}\text{O}^{2-}\text{Sb}^{5+}$  charge-transfer complexes, in which oxygen acts as the interconnecting ligand.

**Acknowledgment.** We thank A. Kornowski for TEM and J. Kolny and XRD measurements. Fruitful discussions with Dr. M. Haase are also acknowledged. This work was partially financed by the Dornier Research Laboratories and the Fond der Chemischen Industrie.

## References and Notes

- (1) Boschloo, G.; Fitzmaurice, D. *J. Phys. Chem. B* **1999**, *103*, 3093.
- (2) zum Felde, U.; Haase, M.; Weller, H. *J. Phys. Chem. B* **2000**, *104*, 9388.
- (3) McGinley, C.; Al Moussalami, S.; Riedler, M.; Pflughoeft, M.; Borchert, H.; Haase, M.; de Castro, A.; Weller, H.; Möller, T. *Eur. J. Phys. D* **2001**, *16*, 225.
- (4) McGinley, C.; Borchert, H.; Pflughoeft, M.; Al Moussalami, S.; de Castro, A.; Haase, M.; Weller, H.; Möller, T. *Phys. Rev. B* **2001**, *64*, 245312.
- (5) Goodman, J. F.; Gregg, S. J. *J. Chem. Soc.* **1960**, 237, 1162.
- (6) Orel, B.; Lavrencic-Stangar, U.; Crnjak-Orel, Z.; Bukovec, P.; Kosec, M. *J. Non-Cryst. Solids* **1994**, *167*, 272.
- (7) Vincent, C. A.; Weston, D. G. C. *J. Electrochem. Soc.* **1972**, *119*, 518.
- (8) Coleman, J. P.; Lynch, A. T.; Madhukar, P.; Wagenknecht, J. H. *Solar Energy Mater. Solar Cells* **1999**, *56*, 375.
- (9) Orel, B.; Lavrencic-Stanger, U.; Kalcher, K. *J. Electrochem. Soc.* **1994**, *141*, L127.
- (10) Olivi, P.; Pereira, E. C.; Longo, E.; Varella, J. A.; Bulhoes, L. O. d. S. *J. Electrochem. Soc.* **1993**, *40*, L81.
- (11) Rockenberger, J.; zum Felde, U.; Tischer, M.; Tröger, L.; Haase, M.; Weller, H. *J. Chem. Phys.* **2000**, *112*, 4296.
- (12) Atkinson, L.; Day, P. *J. Chem. Soc. A* **1969**, 2423.
- (13) Robin, M. B.; Day, P. *Adv. Inorg. Chem. Radiochem.* **1967**, *10*, 247.
- (14) Weinland, R. F.; Schmid, H. *Ber. Dtsch. Chem. Ges.* **1905**, *38*, 1080.